



Jet Propulsion Laboratory
California Institute of Technology



TECHNOLOGY DEVELOPMENT FOR EXOPLANET MISSIONS

TECHNOLOGY MILESTONE WHITE PAPER Optimal spectrograph and wavefront control architectures for high-contrast exoplanet characterization

Dimitri Mawet, Caltech/JPL
Nemanja Jovanovic, Caltech
Jorge Llop Sayson, Caltech
Garreth Ruane, JPL/Caltech
AJ Riggs, JPL/Caltech
Carl Coker, JPL/Caltech
Chris Stark, STScI
Stuart Shaklan, JPL/Caltech
Bertrand Mennesson, JPL/Caltech

May 19, 2020

National Aeronautics and Space Administration
Jet Propulsion Laboratory
California Institute of Technology
Pasadena, California
© 2020 copyright. All rights reserved



Jet Propulsion Laboratory
California Institute of Technology



Approvals

Released by:

Dimitri Mawet
Principal investigator

Date

Approved by:

Brendan Crill
Exoplanet Exploration Program Deputy Chief Technologist

Date

Nick Siegler
Exoplanet Exploration Program Chief Technologist

Date

Douglas Hudgins
Exoplanet Exploration Program Scientist

Date

Table of content

1 Objective	3
2 Wavefront Control and Single-Mode Fibers	5
3 Milestone definition	8
4 Error budget	9
5 Relevance for a Future Exoplanet Mission and TRL	10
6 Testbed descriptions	11
6.1 The High Contrast Spectroscopy Testbed at Caltech	11
6.2 The Decadal Survey Testbed at JPL	13
6.3 Differences Between Flight and Laboratory Demonstrations	14
7 Data Measurement and Analysis	16
7.1 Definitions	17
7.2 Measurements of star brightness	19
7.3 Measurements of contrast	20
7.4 Milestone demonstration procedure	20
7.5 Milestone data package	20
8 Success Criteria	22
9 Schedule	23
10 References	24

TECHNOLOGY MILESTONE WHITE PAPER

Optimal spectrograph and wavefront control architectures for high-contrast exoplanet characterization

1 Objective

We aim to explore and demonstrate optimal spectrograph and wavefront control architectures for high-contrast exoplanet characterization with future space-based observatories. Once a candidate exoplanet has been imaged and its position measured, follow-up spectroscopy over a wide range of wavelengths and spectral resolutions is necessary to characterize its atmosphere in detail (Figure 1). According to the most recent Design Reference Missions for WFIRST CGI, HabEx and LUVOIR, the time required for spectroscopic characterization with internal coronagraphs is typically two orders of magnitude larger than for detection, which can become prohibitive. Indeed, exposure times for spectroscopy in a single 20% bandpass approach one month in time, during which the planet orbits and may disappear. Thus obtaining full spectra over multiple bandpasses serially becomes operationally implausible (Figure 2). To mitigate this issue, the HabEx Science and Technology Definition Team (STDT) has chosen a hybrid coronagraph plus starshade architecture (Gaudi et al. 2018). The nimble internal coronagraph is primarily used for detection and orbit characterization using imaging over two 20% bandwidth channels. When a promising exoplanet candidate is found, the starshade is slewed into place to undergo detailed spectroscopic characterization over the entire passband of the instrument (covering the optical and near-infrared wavelengths). Because the starlight suppression is offloaded to an external spacecraft, the starshade spectrograph instrument can be much simpler resulting in 2-4 times higher planet throughput. The starshade's stellar suppression is almost achromatic over its wide operating bandpass, making spectral characterization over a full octave possible and complementary to the nimble coronagraph.

However, the HabEx STDT team has been studying a coronagraph-only architecture (HabEx C) to mitigate risks and cost associated with the more complex and expensive hybrid mission. In that scenario, we have to rely on the internal coronagraph for spectral characterization. Similarly, the LUVOIR (The LUVOIR Team 2018) baseline architecture relies on internal coronagraphs alone, since the larger LUVOIR telescope diameter (9-15 meter) yields very large starshade sizes. For a fixed inner working angle, the required starshade diameter scales with telescope diameter. Therefore, both HabEx C and LUVOIR require optimized spectrograph and wavefront control architectures for high-contrast exoplanet characterization.

The metrics used to optimize instrument and wavefront control architectures for exoplanet searches are however sub-optimal for follow-up spectroscopy. Indeed, planet searches necessitate large dark holes to be cleared out of residual starlight and put a strain on the wavefront control system that results in contrast, throughput and bandwidth trade-offs. However, once the position of the planet is known, wavefront control degrees of freedom can be re-allocated by reducing the dark hole size and used to improve contrast, throughput and bandwidth (Borde & Traub 2006, Coker et al. 2019A, Potier et al. 2020), potentially reducing the

spectroscopic exposure time by orders of magnitude. Moreover, we recently showed that the use of single-mode fibers to feed the planet light to a single- or few-object spectrograph can also lead to substantial gains in efficiency (Mawet et al., 2017; Llop Sayson et al., 2019; Coker et al., 2019A/B). Our proposed program will explore the dark hole size, contrast, throughput, and bandwidth trade space by undergoing detailed end-to-end numerical simulations and laboratory demonstrations in the Exoplanet Technology Lab and High Contrast Spectroscopy Testbed (HCST) at Caltech, as well as the Decadal Survey Testbed (DST) at JPL. Section 2 describes the latest simulation and laboratory results for wavefront control and the use of single-mode fibers in more detail.

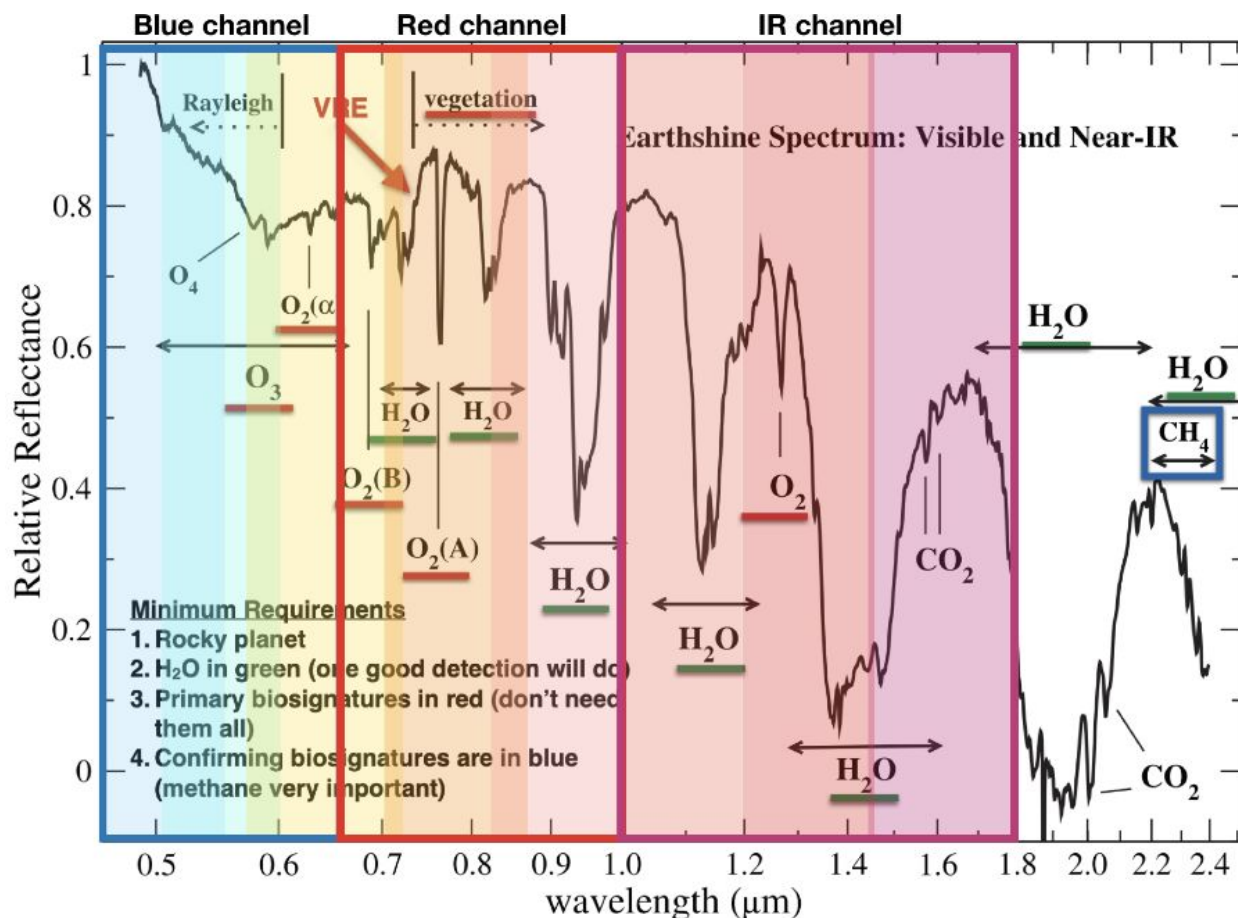


Figure 1: Earth-like spectrum and main biosignatures over the passband covered by HabEx and LUVOIR (Rauscher et al., 2015). The overlaid colored rectangles represent the eight 20% bandpass filters of HabEx required to cover the visible and near-IR spectral range. These are divided into three main camera channels: blue, red, and IR.

The nominal wavelength range for exoplanet spectroscopy selected by HabEx and LUVOIR includes optical and near-infrared bandpasses from 0.5 μm to 1.8 μm (HabEx), and 2 μm (LUVOIR). This wavelength range covers most if not all biosignatures of interest (Figure 1). The typical maximum bandwidth of high-contrast coronagraph operations has currently been limited to 20% (Trauger et al. 2011). This practical limitation is the result of coronagraph mask

technologies used so far and the ability to control wavefront errors over large bandwidths and typical large dark hole sizes used for discovery and orbit characterization. New coronagraph designs such as optimized apodized pupil Lyot, shaped pupil and vector vortex coronagraphs are now in principle capable of covering up to an octave or 50% bandwidth (Mawet et al., 2011; Soummer et al., 2011; Balasubramanian et al., 2015; Serabyn et al., 2019), so the primary limitation to bandwidth becomes wavefront control (Krist et al. 2008).

Dark hole sizes are usually set by the number of actuators on the deformable mirror with the control radius limited to $N/2 \lambda/D$, where N is the number of actuators across the pupil. In discovery/planet search mode, the wavefront control system is naturally optimized to provide the largest possible field of view, so all of the degrees of freedom provided by the deformable mirror ($\sim N^2$) are allocated to spatial modes. Krist et al. (2008) noted early on that dark hole sizes could be reduced to improve contrast and bandwidth, and this trade-off is currently exploited to some extent for the WFIRST CGI (Krist et al. 2018).

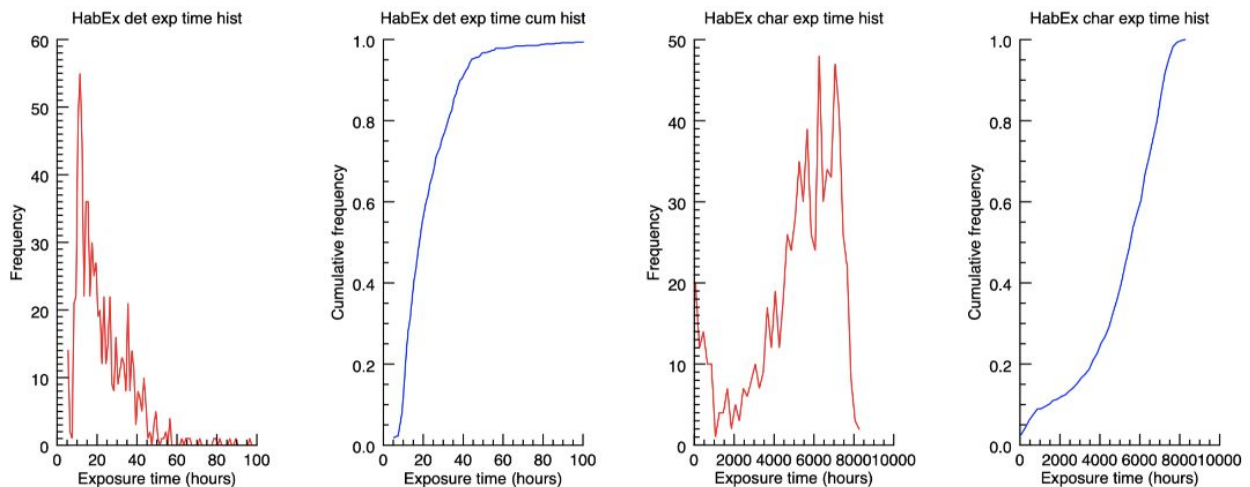


Figure 2: Histogram and cumulative distribution of exposure times for detection and characterization for the HabEx mission as derived from the yield assessment using AYO (Stark et al., 2016). The cumulative exposure times for spectroscopy assume serialized observations through the full bandpass of HabEx.

2 Wavefront Control and Single-Mode Fibers

Active wavefront control is key to the success of any coronagraphic mission which hopes to directly image Earth-like exoplanets. There have been several approaches to this problem which have been studied over the years (see, e.g., Give'on et al. 2007, Pueyo et al. 2009, Miller et al. 2017), but the most relevant to our research is electric field conjugation, or EFC (Give'on et al., 2007). In EFC, the electric field is measured at the instrument focal plane, and then an optical propagation model of the instrument is used along with the effect of known perturbations of each actuator on the deformable mirrors to derive the actuator heights required to correct the phase and amplitude errors in the image plane.

It has long been established that shrinking the size of the dark hole, or somewhat equivalently, increasing the number of actuators on the deformable mirror while keeping the dark hole the

same size, improves the achievable contrast, and that this contrast can then also be traded off against other important observational parameters such as throughput and bandpass (Borde & Traub 2006, Krist et al. 2008, Beaulieu et al. 2017, Coker et al. 2019A, Potier et al. 2020). Improvements in contrast range from a factor of ~ 2 to several orders of magnitude, depending on the wavefront control algorithm used and how small the dark hole becomes.

Further improvements can be generated by using a single-mode fiber for wavefront control. Over the past four years, we have been investigating the potential applications of single-mode fibers to coronagraphic exoplanet detection and characterization (Mawet et al. 2017; Llop Sayson et al., 2019; Coker et al., 2019A/B). In both simulations and experimental lab results, we have seen promising indications that using single-mode fibers can increase the efficiency of spectroscopic observations through a coronagraph by increasing the spectral bandwidth which may be imaged at one time and by improving contrast and usable throughput, particularly in background-limited cases (Coker et al. 2019A).

Mawet et al. 2017 was the first to show the benefits of single-mode fibers for speckle suppression in the lab, finding an improvement in contrast by a factor of ~ 1000 compared to not using a fiber when using a speckle nulling approach. Llop Sayson et al. 2019 was able to demonstrate the use of EFC on the output of a single-mode fiber. Instead of attempting to zero the electric field in the image plane, fiber EFC seeks to minimize the intensity at the output of a single-mode fiber placed in the focal plane by minimizing the overlap integral between the incoming residual starlight and the fiber's propagation mode, thus nulling the coupling of the starlight into the fiber. Moving to fiber EFC resulted in a contrast improvement of a factor of ~ 30 over digging a small conventional dark hole on Llop Sayson et al.'s apparatus, with the promise of further gains with improved equipment and a more accurate model of their coronagraph.

Simulations using multiple fibers simultaneously have also yielded promising results. Coker et al. 2019A investigated the prospect of using five single-mode fibers to take spectra of all exoplanets discovered in a multi-planetary system simultaneously, finding that using single-mode fibers had the potential to double or triple the usable spectral bandpass, depending on coronagraph type (a 10% bandwidth imaging shaped pupil Lyot coronagraph/SPLC was capable of 30% bandwidth when using fibers; Figure 3). In addition, as single-mode fibers are capable of producing very deep nulls when used as an integral part of the wavefront control system, the requirements on the coronagraph mask can be relaxed, potentially resulting in an improvement in coronagraph throughput ($\sim 35\%$ increase seen for SPLCs) as well as a further improvement in bandpass (from 30 to 35% using SPLCs).

Further simulations in Coker et al. 2019B using 3 cores of a multi-core fiber and a model of the HCST bench with an achromatic vector vortex coronagraph indicate that bandwidths of at least 40% are possible with contrast between the $1e-8$ and $1e-9$ levels across the band (Figure 4). These simulations use a realistic wavefront control and measurement strategy including pairwise probing and the limitations of the DM electronics.

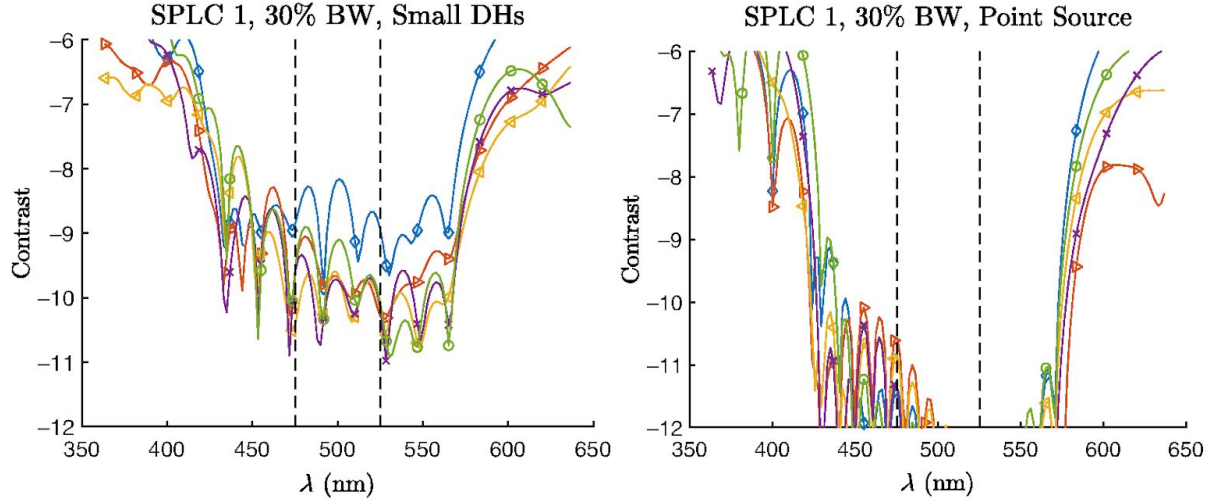


Figure 3: Contrast results of a simulation from Coker et al. 2019A using a SPLC mask designed to achieve $1e-10$ contrast over a 10% bandwidth in imaging mode. The left panel shows the results of using five small dark holes which are each $3 \lambda/D$ across, while the right panel shows the effects of using five single-mode fibers instead in the same locations. The model is able to achieve $1e-10$ contrast or better across a 30% bandwidth with the fibers, something which is not possible using small dark holes alone.

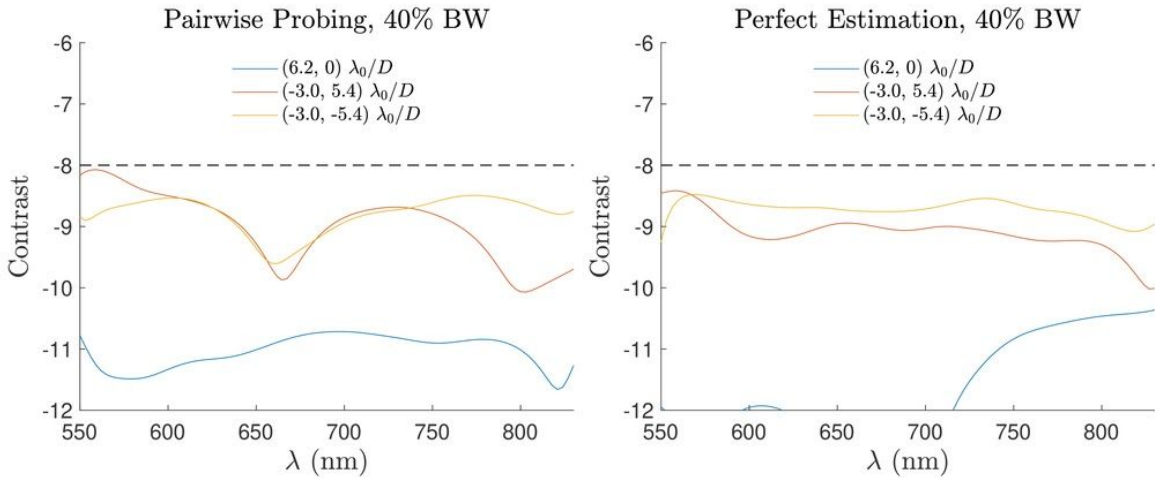


Figure 4: Contrast results of simulations from Coker et al. 2019B of the HCST bench with an achromatic vector vortex coronagraph mask and a multi-core fiber, with 3 cores controlled. Each line represents the contrast vs. wavelength curve for one core, with their positions relative to the center of the field given in the legend. The left panel shows the results of using pairwise probing to estimate the electric field, while the right panel shows the results of assuming perfect knowledge of the field. The fact that the pairwise probing results are substantively identical to the perfect estimation results is encouraging for our prospects of achieving spectral bandwidths this large ($\sim 40\%$).

3 Milestone definition

SAT Technology Milestones are intended to document progress in the development of key technologies for a space-based mission that would detect and characterize exoplanets, such as Exo-C, Habex and LUVOIR, thereby gauging the mission concept's readiness to proceed from pre-Phase A to Phase A.

#	Date	BW	Raw Contrast	Configuration	Facility	Note
1	03/21	20%	1e-8	1 Object & 1 Single Mode Fiber (SMF)	HCST	Best result so far on the HCST is 4e-8 in 10% BW over a half dark hole
2	06/21	30%	1e-8	1 SMF	HCST	
3	12/21	30%	1e-8	Multi-SMF (≥ 2)	HCST	
4	03/22	10%	4e-10	1 Object	DST	Best result so far on the DST is 4e-10 in 10% BW, the goal here is to reproduce this contrast result for a single object before moving on to larger BW
5	06/22	20%	4e-10	1 Object	DST	
6	09/22	20%	4e-10	Multi-Object (≥ 2)	DST	

Table 1. Project milestones.

A first series of pre-milestone will be performed in year 1 through numerical simulations, to inform the prospects of the subsequent laboratory demonstration milestones. The goal is to perform a tolerance analysis of the end-to-end system, looking for potential pitfalls and breaking points, and adapt the wavefront control strategy accordingly. These simulations will help prepare the subsequent laboratory demonstrations, and design the single-mode and multi-core single-mode fiber injection hardware.

Milestone #1: 20% BW demonstration of a small $2 \lambda/D \times 2 \lambda/D$ 1e-8 dark hole (1 object) on the Caltech HCST.

Milestone #2: 30% BW demonstration of 1e-8 nulls through a SMF (1 object) on the Caltech HCST at three distinct locations in the control radius of the wavefront control system.

Milestone #3: 30% BW demonstration of multiple (≥ 2) $1e-8$ nulls simultaneously through a multi-core SMF at distinct locations in the control radius of the WFC system on the Caltech HCST.

Milestone #4: 10% BW demonstration of a small $2 \lambda/D \times 2 \lambda/D$ $4e-10$ dark hole (1 object) on the DST at JPL. The goal is to re-establish the baseline performance of DST (currently $4e-10$ over 10% BW) and improve upon it using a small dark hole.

Milestone #5: 20% BW demonstration of a small $2 \lambda/D \times 2 \lambda/D$ $4e-10$ dark hole (1 object) on the DST at JPL.

Milestone #6: 20% BW demonstration of multiple (≥ 2) small $2 \lambda/D \times 2 \lambda/D$ $4e-10$ dark holes at distinct locations within the WFC system control radius on the DST at JPL.

4 Error budget

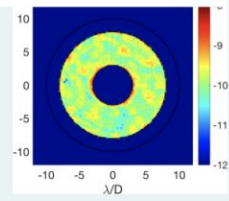
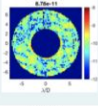
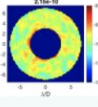
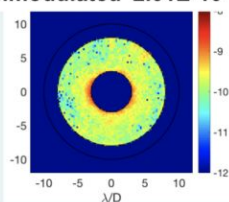
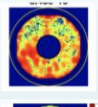
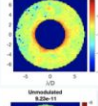
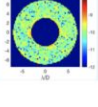
Contrast, 3.82E-10 Total		Measured	Model/Indirect Expectation	Morphology	
Modulated 1.81E-10 	LSB effect of DM actuators	8.78E-11	$\sim 1E-10$	Specklish	
	Chromatic Control Residual	9.32E-11	$\sim 4E-11$	Specklish	
Unmodulated 2.01E-10 	Occluder Ghost (+Chromatic Residual)	1.01E-10	$\sim 1E-10$	Patterned March with wavelength	
	Testbed LoS Jitter impact	4.19E-11	$< 1E-11$	Centered	
	Unknown	5.04E-11	N/A	Diffused	

Table 2. DST error budget reproduced from Seo et al. 2019.

Our error budget strategy is to follow the current best practices, informed by recent experience on the DST (Table 2). During the first year, the error budget will be populated by our planned simulation work, and then validated against experimental results in subsequent years.

The error budget for the DST was empirically determined by the HCIT team during the DST commissioning using pairwise probing to differentiate between modulated and unmodulated components of the residual field in the dark hole (see Table 2). For example, the impact of the quantization errors in the DM electronics (“LSB effect of DM actuators” in Table 2) is estimated from the modulated component when using monochromatic light. The change in the modulated component when changing from a monochromatic laser source to 10% bandwidth is called the

Chromatic Control Residual (CCR), which accounts for $\sim 1e-10$ of the error budget at 10% bandwidth.

Using a small dark hole may reduce the CCR term significantly, in which case the contrast limit for DST will be $\sim 3e-10$. The milestones listed above aim to test this hypothesis by achieving an equivalent CCR to the 10% bandwidth case during commissioning, but over a 20% bandwidth by reducing the dark hole size and only addressing locations of known source objects of interest.

The incoherent components account for $\sim 2e-10$ of the error budget, which are likely impossible to reduce without improving the testbed hardware.

5 Relevance for a Future Exoplanet Mission and TRL

Enabling super-broadband coronagraph operations for spectroscopic characterization with internal coronagraphs will boost the efficiency of HabEx and LUVOIR's coronagraph instruments, potentially by several orders of magnitude. The only prerequisite is that the planet is detected using the nominal imaging/search mode, and its position known within a fraction of a resolution element (typically $< 0.2 \lambda/D$, consistent with HabEx's astrometric precision of 5 mas rms and requirements for orbit determination, see Section 3.1.1.2 in the Public HabEx Final Report). This capability is particularly critical for HabEx's architecture C (coronagraph only), and LUVOIR, which cannot rely on a companion starshade for broadband spectroscopic characterization.

As mentioned before (Section 2), trading off WFC degrees of freedom between contrast, dark hole size, bandwidth and throughput have been applied to various high contrast concepts and in particular to the WFIRST CGI, where, e.g., the SPC has been the favored high bandwidth spectroscopic mode (TRL 5). Our proposal is to push the trade-off to extremely small size dark holes to maximize characterization spectral bandwidth, with and without the use of SMFs. The starting TRL of this project is 3, i.e. it has been validated in numerical simulations (Section 2) and demonstrated at the proof-of-concept level in Mawet et al. 2017. Our aim is to bring the concept to TRL 4 (breadboard validation on the HCST), then TRL 5 on the DST (in a vacuum environment).

6 Testbed descriptions

6.1 The High Contrast Spectroscopy Testbed at Caltech

The High Contrast High-Resolution Spectroscopy Testbed (HCST; Jovanovic et al., 2018), in the PI's Caltech Exoplanet Technology Lab (ETL) is aimed at filling a gap in technology development for future exoplanet missions, and providing the US community with an academic facility to test coronagraph, spectroscopy, and wavefront control technologies for future large ground-based and space-based telescopes (Figure 3). The goal of HCST is multi-fold and addresses high-contrast direct imaging and spectroscopy of exoplanets from space in support of LUVOIR, HabEx (and, accessorially in this context, the Thirty Meter Telescope/TMT).

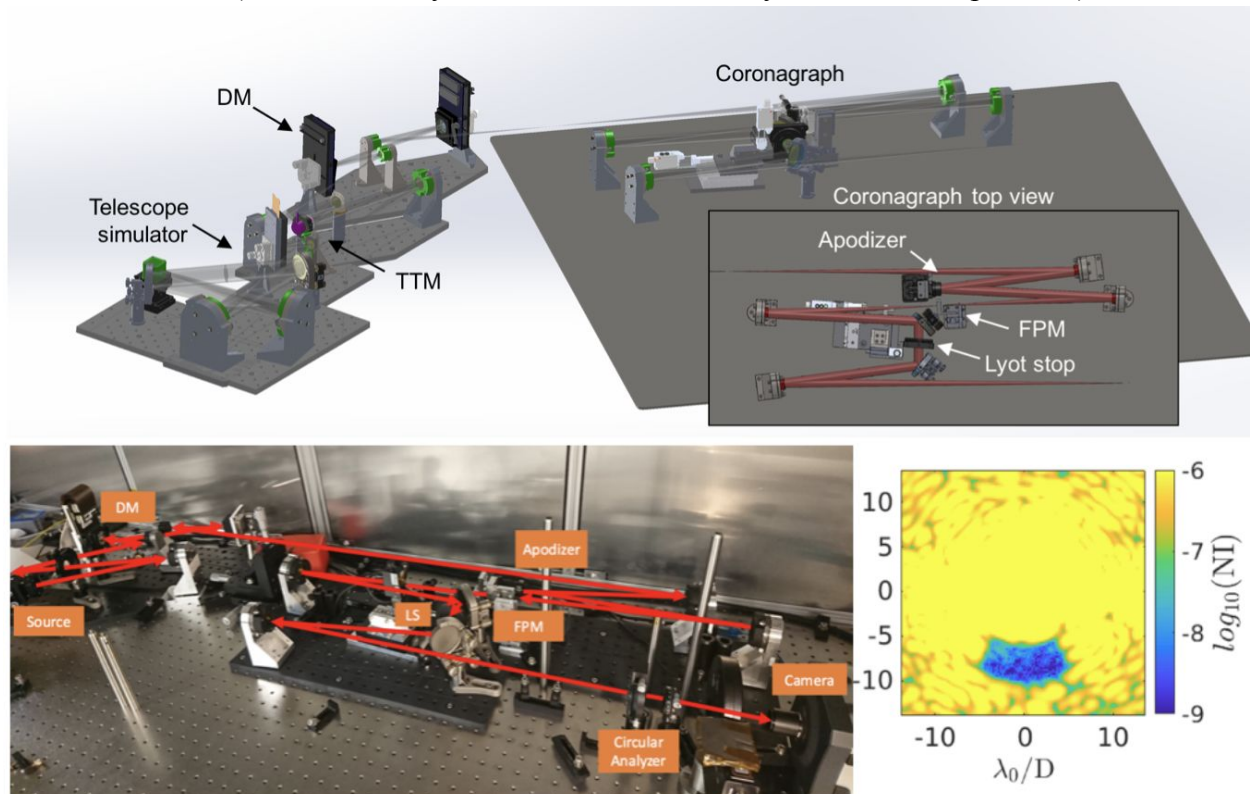


Figure 3. Top: HCST CAD model showing the telescope simulator on the left, followed by the wavefront control system, and the coronagraph. Bottom left: annotated picture of the HCST. Bottom right: $1e-8$ monochromatic (2% BW) dark hole.

HCST includes two NKT super-continuum white-light lasers with an NKT VARIA tunable single line filter, which allows us to precisely scan in wavelengths and define arbitrary bandwidths in the visible. Our baseline design contains the telescope simulator, a downstream wavefront corrector, which includes one Boston Micromachine (BMC) kilo-DM (32×32 actuators), followed by a classical 3-plane single-stage coronagraph (entrance apodizer, focal-plane mask, Lyot stop), and an imaging camera (Neo sCMOS). We have a series of achromatic vector vortex focal plane masks with topological charges from 2 to 8. Our facility is also equipped with a fiber-fed optical spectrum analyzer (Thorlabs OSA202C covering the 600 - 1700 nm range, with -65 dBm/nm (600 - 700 nm) and -70 dBm/nm (700 - 1700 nm) noise floors)

which will be used to analyze the chromaticity of our wavefront control solutions and compare them to theory. The HCST is now operational (Llop-Sayson et al., 2019). We recently achieved a half (10% bandwidth) dark hole with raw contrast of $1e-8$ (Figure 5, bottom right).

The HCST facility in the Caltech ETL is currently funded by various internal sources at Caltech and JPL, so here we only request funding for hardware necessary to conduct our experiment, described below.

Planet-star simulator. For this demonstration, we propose to generate planet and star signals and launch them simultaneously on the testbed so planet throughput and raw contrast can be verified contemporaneously. The requirement for the planet star simulator is to produce two point sources with adjustable separation ($2-15\lambda/D$ angular separation) and flux ratio in the range $1e-8$ to $1e-9$. For that, we propose to assemble a planet-star simulator based on a prototype recently built and proof-tested for another experiment (Mawet et al., 2017). The simulator consists of two independent light sources (NKT Super K super-continuum white light sources covering the 390-2400 nm wavelength range and including an NKT VARIA tunable filter), one of which is passed through a beamsplitter and the other reflected off of the beamsplitter, to create a source with two co-propagating beams. Since the light sources are independent, we ensure mutual incoherence and sufficient flexibility to set the flux ratio between the two beams. Additional pinhole filtering can also be provided to each beam if necessary.

Fiber injection unit. We propose to build a new fiber injection unit (FIU) to link the coronagraph instrument and the spectrograph (Figure 6). The purpose of the FIU is to couple planet light into a single mode fiber (SMF) and maintain accurate alignment throughout long-exposure observations (up to several hours). The pointing accuracy and stability is achieved through active sensing and control of the planet and fiber positions using a robust architecture inherited from and leveraging two decades of technology developments in stellar interferometry (Colavita et al., 1999). An actuated tip-tilt mirror (TTM) is used to align the planet image position with the tip of the SMF, whose relative locations are determined by simultaneously imaging the scene and the SMF with a tracking camera. A beamsplitter (BS) or dichroic reflects part of the science beam to the tracking camera directly after the TTM. To locate the SMF, a calibration source (CAL) is retro-fed through the fiber, for instance, by means of Y-couplers. The BS reflects light from the SMF towards a corner cube (CC) retroreflector, which sends the beam back through the BS and towards the tracking camera. A beacon image is formed on the tracking camera at the location of the SMF. The beacon is used to determine the TTM settings to co-align the object image and the SMF. Alternatively, the CAL source may feed a separate SMF creating a beacon near the spectrograph fiber tip so the relative positions can be calibrated. The FIU is also designed to provide feedback mechanisms for starlight suppression using the upstream deformable mirror (DM). A low-noise single pixel detector (e.g. an avalanche photodiode; APD) may be used to monitor the starlight leaking into the fiber at high-speed and drive a control loop that minimizes leaked starlight in real time. We have demonstrated both the optical alignment procedure and real time wavefront control concepts in the laboratory (Mawet et al., 2017; Llop Sayson et al., 2019).

Fiber bundling and multi-core fibers. To demonstrate the multiplexing capabilities of the new wavefront control strategy, we will acquire a combination of single-mode fiber bundles and/or multi-core fibers of various configurations. Regardless of the type of bundle architecture, we will adjust the system such that a single mode fiber core subtends $1 \lambda/D$ in the focal plane. Multi-core fibers are convenient because they support all cores in a single cladding making them simpler to construct and handle. However, multi-core fibers have a minimum core separation of about $5-6 \lambda/D$ which do not offer the ability to sample the field as we would like. Nonetheless they can be useful for initial tests and will be purchased from Chiral Photonics. By virtue of placing micro-lens arrays on the front of a fiber bundle, it's possible to increase the fill factor and hence minimize the spacing between neighbouring cores. After an initial demonstration with a bare multi-core fiber, we will purchase a fiber bundle from Fiberguide Industries with micro-lens arrays attached that will have a fiber spacing of $1\lambda/D$.

6.2 The Decadal Survey Testbed at JPL

DST is a new, advanced testbed that consists of a stellar source simulator, two deformable mirrors (either 48×48 Xinetics or 50×50 BMC) for wavefront control, coronagraph masks, a wavefront sensor, and an imaging camera (Figure 4). DST's opto-mechanical design minimizes disturbances from the laboratory and local environment. At its foundation, DST consists of a carbon-fiber optical table that is highly stable to thermal fluctuations and includes active temperature control. Vibration isolators reduce the sensitivity to seismic and laboratory vibrations. An active steering mirror can actively correct for residual tip/tilt errors while the two DMs correct other imperfections in the optical wavefront. All of the optics are highly polished and reflective where possible to minimize wavelength-dependent aberrations. The entire testbed is housed inside of a 12-meter long vacuum chamber to eliminate effects of the atmosphere. As of March 2019, the DST team achieved a mean raw contrast of $4e-10$ averaged over angular separations $3-9 \lambda/D$ with a bandwidth of $\Delta\lambda/\lambda=0.1$ about $\lambda=550$ nm using a Lyot coronagraph in a single polarization. With the same setup in monochromatic light, the deepest raw contrast was $2e-10$ with the same dark hole region.

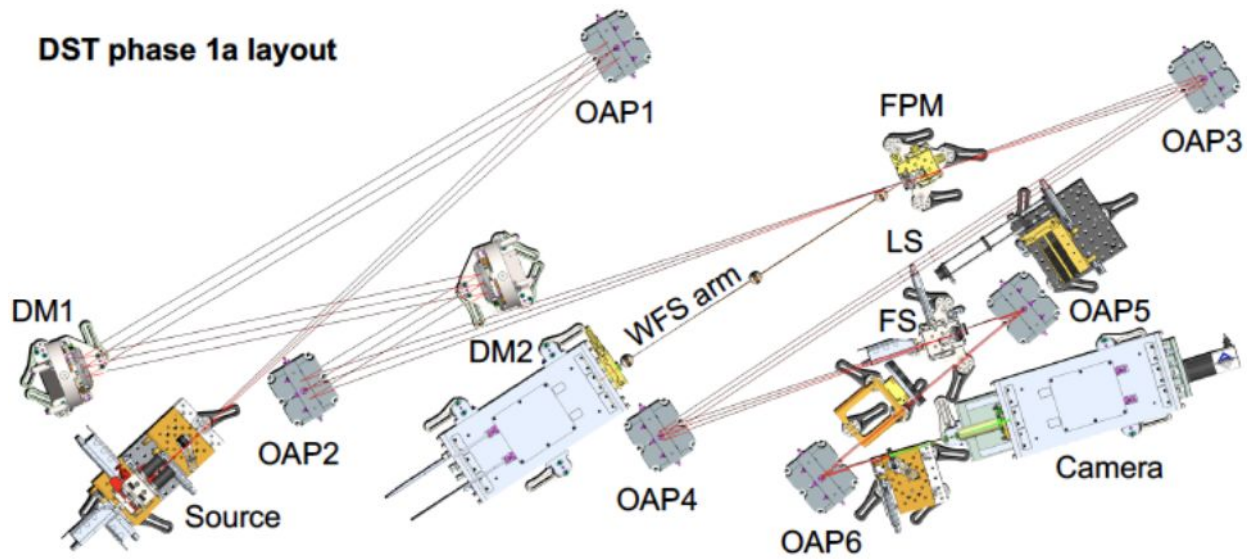


Figure 4: Optical layout of DST. OAP = off-axis paraboloidal mirror. DM = deformable mirror. FPM = focal plane mask. LS = Lyot stop. FS = field stop.

6.3 Differences Between Flight and Laboratory Demonstrations

Although the coronagraph layouts in the laboratory are conceptually the same as is being proposed for future flight implementations on exoplanet space missions such as Habex, LUVOIR, there are several differences:

Light intensity: In a space coronagraph, the spectrum of light illuminating the coronagraph would closely resemble black body radiation, while for these milestones, the source will be a broadband super-continuum source filtered to the desired bandwidth. This source provides a photon flux that is comparable to or somewhat brighter than the target stars to be observed. The goal of these milestones is to demonstrate the contrast and bandwidth gain that can be achieved with a small dark hole or SMF at the location of the planet, independent of the source intensity. A bright source is a convenience that does not compromise the integrity of the demonstration, as it affects only the integration times.

Light spatial uniformity: Unlike the light incident on a telescope from a target star, the light intensity in the testbeds is not uniform across the pupil. Typically, the light intensity drops center-to-edge by a few percent, due to the diffraction pattern from the small source pinhole. This small non-uniformity is expected to have a negligible effect on the final contrast if it is accounted for in the wavefront control algorithm, and a small but below- requirement loss of contrast if it is ignored in the control algorithm.

Number of polarization states: The experiments proposed here will be done in single polarization. Our input polarizer will be located upstream of the pinhole, which is not where it

would be in a flight system; in that case, it would need to be located in a more spatially extended beam. We note that our experience has shown that the location of the polarizer upstream of the pinhole is sufficient to enable polarization control at the FPM and its difference of location w.r.t. where it will be in the flight system, will not affect the validity of our results.

Number of deformable mirrors: Both in the laboratory and in space, the highest contrasts call for two DMs in the optical system, in order to allow for the control of both phase and amplitude errors in the complex wavefront over one half of the coronagraphic field described. A pair of DMs may also be used in series to generate a full two-sided dark hole, and can provide better broadband control through the use of the Talbot effect. The DST makes use of a pair of DMs, as is planned for future high-contrast space missions, and is thus essential to meeting our contrast requirements.

Spacecraft dynamics: A control system is required in flight to stabilize the light path against motions of the spacecraft. The dominant effects of spacecraft dynamics are jitter of the star image on the coronagraphic focal plane mask and beam walk in the optics upstream of the focal plane mask. For a specific example, the ACCESS analysis (Trauger et al. 2010) showed that for fourth-order coronagraphs (including Lyot, vortex, and pupil mapping coronagraphs) with an inner working angle of $3 \lambda/D$, rms pointing errors need to be $< \pm 0.03 \lambda/D$ to limit the contrast degradation to $< 2e-10$. The concept models have shown that the required pointing stability can be achieved in space with current high Technology Readiness Level (TRL) systems. In the DST, this would correspond to an ability to center the coronagraphic mask on the “star” within about $2.5 \mu\text{m}$, or about 0.2 pixel when projected to the CCD focal plane.

The milestone demonstration requires passive stability of the testbed, which is thus untraceable to spacecraft dynamics. In practice, DST may exhibit alignment drifts that are larger than expected in the space environment. If so, we will rely on favorable periods of thermal and mechanical stability of DST.

7 Data Measurement and Analysis

A contrast measurement is a measurement of the intensity of the residual light (speckles, background, etc.) within the dark field (resp. through a SMF), relative to the peak intensity of an image of the source (resp. through a SMF). There will of course be a distribution of intensities across the dark hole (irrelevant for a SMF), from which the average contrast and its statistical confidence level will be calculated. The milestone objective is to demonstrate with high confidence ($\geq 90\%$) that the true contrast in the dark field (resp. through a SMF), as estimated from our measurements in the presence of noise, is equal to or better than the required threshold contrast.

Because of laboratory instabilities and the currently used wavefront control algorithms, the contrast at any point in the dark field (resp. through a SMF) is time dependent, and so multiple successive exposures of the dark hole will be taken. For each image (where “each image” can itself be more than one sequential image if temporal averaging is deemed important to build up signal to noise), we calculate a spatial average of the measured contrast level over the entire dark hole (irrelevant for a SMF). This yields a series of n (with $n \geq 4$) individual dark hole images, each with its own spatially-averaged dark hole contrast, c_i . We next take an average over the series of n dark hole images, leading to a sample-averaged contrast and variance, both defined below. To avoid confusion, we refer to spatial averages over an image region as “averages”, and averages of quantities over a number (sample) of images as “means”. Finally, we note that the entire experimental run is then to be repeated from scratch at least 3 times, to show repeatability. No averaging is done over the independent runs, so that the milestone is achieved independently m times.

As mentioned, the measured contrast is time dependent, being subject to laboratory conditions such as the quality of the optical components, their alignment, drifts in their alignment over time, and the effectiveness of each wavefront sensing and control cycle. With each iteration, the wavefront sensing and control procedure attempts to improve the contrast, thus compensating for any drift or alignment changes that may have occurred since the previous iteration. Further variations may be expected due to experimental noise and any limitations in the algorithm. The images built up from a sequence of such iterations will provide a distribution of contrast values, which will be regarded as Gaussian about a mean contrast for the data set. We therefore consider the mean contrast value as representative of the true contrast value for a given data set.

The contrast measurements of the iterations within a single run will fluctuate due to both random wavefront control errors and random measurement errors. The statistical confidence level will thus require an estimation of the variance. Given that our speckle fields contain a mix of static and quasi-static speckles (the residual light field remaining after the completion of a wavefront sensing and control cycle, together with the effects of alignment drift following the control cycle), as well as other sources of measurement noise including photon detection statistics and detector read noise, an analytical development of speckle statistics is impractical. We will thus compute the confidence levels under the assumption of Gaussian statistics. (The full set of

measurements will also be stored, to enable computation of the confidence levels for other statistics.)

The following paragraphs define the terms involved in the measurement process, spell out the measurement steps, and specify the data products.

7.1 Definitions

7.1.1. “Raw” Image and “Calibrated” Image. Standard techniques for the acquisition of sCMOS images are used. A “raw” image is the pixel-by-pixel image obtained by reading the charge from each pixel of the sensor, and amplifying and sending it to an analog-to-digital converter. A “calibrated” image is a raw image that has had a background bias subtracted and the detector responsivity normalized by dividing by a flat-field image. (Saturated images are avoided in order to avoid the confusion of sensor blooming and other potential sensor nonlinearities.) A calibrated image can also include the step of low-order aberration contribution subtraction based on wavefront information provided by a low-order wavefront sensor, if one is available).

7.1.2. “Scratch” is a DM setting in which actuators are set to a predetermined surface figure that is approximately flat (typically, about 20 volts on each actuator).

7.1.3. The “algorithm” is the computer code that takes as input the measured speckle field images, and produces as output a voltage value to be applied to each element of the DM, with the goal of reducing the intensity of speckles.

7.1.4. The “star” is a small pinhole illuminated with laser or broadband light relayed via optical fiber from a source outside the chamber’s vacuum wall (e.g., a laser or a filtered super-continuum white light source). The “small” pinhole is to be unresolved by the optical system; e.g., a 5- μm diameter pinhole would be “small” and unresolved by the 80- μm FWHM Airy disk in an $f/100$ beam at 600 nm wavelength. This “star” is the only source of light in the optical path of the coronagraph. It is a stand-in for the star image that would have been formed by a telescope system.

7.1.5. The “contrast field” is a dimensionless map representing, for each detector pixel, the ratio of its value to the value of the peak of the PSF that would be measured in the same testbed conditions (light source, exposure time, Lyot stop, etc.) if the coronagraphic mask were removed. The calibration of the contrast field is discussed in Section 7.3.

7.1.6. The “average contrast”, c_i , is a dimensionless quantity that is, for a given image, the spatial average value of the contrast field over the defined dark hole. Explicitly, an image’s average contrast is the sum of the contrast values for all pixels in the dark field, divided by the total number of pixels in the dark field, with no weighting applied.

7.1.7. The “SMF contrast” is a dimensionless number representing ratio of the intensity value measured at the output of the SMF placed in the speckle field by the intensity value measured at the output of the SMF placed on the peak of the PSF when measured in the same testbed conditions (light source, exposure time, Lyot stop, DM settings, etc.) if the vortex mask were

removed. The use of this metric, as opposed to normalizing by the total stellar brightness, is a key indicator of the overall performance of the wavefront control system. The alignment and computation of the peak star intensity through the SMF used to normalize the SMF contrast is described in 7.2.2.b, and the calibration of the contrast field is discussed in Section 7.3.

7.1.8. The “mean contrast”, \hat{c} , of a given sequence of $n \geq 4$ images is the mean of the individual average contrast values occurring in that sequence:

$$\hat{c} = \frac{1}{n} \sum c_i.$$

7.1.9. “Milestone metric”: \hat{c} is the milestone metric.

7.1.10. “Standard Deviation”: The standard deviation σ_{meas} for an individual measurement of the average contrast value c_i of a sequence of contrast images given as usual by:

$$\sigma_{meas} = \sqrt{\sum_{i=1}^n \frac{(c_i - \hat{c})^2}{n - 1}}$$

The uncertainty in the mean contrast \hat{c} is then given by

$$\sigma_{mean} = \frac{\sigma_{meas}}{\sqrt{n}}.$$

There is also a contribution to the uncertainty from the independently-determined photometry error, σ_{phot} . The net standard deviation is thus

$$\sigma = \sqrt{\sigma_{mean}^2 + \sigma_{phot}^2}$$

7.1.11. “Statistical Confidence”. For contrast values that have a Gaussian distribution about the mean contrast, the statistical confidence that the mean contrast \hat{c} is less than some value c_0 is given by

$$\text{conf}(z < t) = \frac{1}{\sqrt{2\pi}} \int_{-\infty}^t e^{-z^2/2} dz = \frac{1}{2} + \frac{1}{\sqrt{2\pi}} \int_0^t e^{-z^2/2} dz$$

where $t = (c_0 - \hat{c})/\sigma$. Thus, as $\hat{c} = c_0 - t\sigma$, meeting a milestone contrast target c_0 with the desired confidence level requires the final measured mean contrast for a given run, \hat{c} , to be lower than the target contrast c_0 by t standard deviations. The Gaussian integral is widely tabulated, and $\text{conf} = 0.9$ implies $t = 1.28$. Thus, for 90% confidence, $\hat{c} = c_0 - 1.28\sigma$, i.e., the measured \hat{c} is smaller than the target c_0 by 1.28σ .

7.2 Measurements of star brightness

7.2.1. The coronagraphic mask is displaced laterally relative to the center of the beam by approximately $10 \lambda/D$ or so, so as to transmit maximum stellar flux.

7.2.2.a. To create the photometric reference, a representative sample of short-exposure (e.g. a few milliseconds) images of the star is taken, with all coronagraph elements other than focal-plane mask in place.

7.2.2.b. To create the photometric reference with the SMF, a representative sample of short-exposure (e.g. a few milliseconds) measurement of the star through the SMF is taken, with all coronagraph elements other than the focal-plane mask in place. To align the star on the SMF, the SMF is back-illuminated, and then the images of the SMF and star are aligned on the tracking camera. This gives a rough position of the star in the SMF plane. A more precise alignment is needed with the FIU stages, with which a scan of the SMF is performed to search for the optimal position of the star.

7.2.3.a. The images are averaged to produce a single star image. The “short-exposure peak value” of the star’s intensity is estimated. Since the star image is well-sampled in the CCD focal plane (the Airy disk can be sampled by ~ 20 pixels within a radius equal to the full width half maximum), the star intensity can be estimated using either the value of the maximum-brightness pixel or an interpolated value representative of the apparent peak.

7.2.3.b. The SMF output measurements are averaged to produce a single star SMF measurement. This value is used to compute the ‘SMF contrast’ as described in 7.1.7. The “short-exposure value” of the star’s intensity through the SMF is estimated.

7.2.4. The “peak count rate” (counts/sec) is measured for exposure times of microseconds to tens of seconds.

7.3 Measurements of contrast

7.3.1. The coronagraphic mask is centered on the star image.

7.3.2. An image with a typical exposure time of several seconds is taken of the coronagraph field (the suppressed star and surrounding speckle field). The target dark hole is a $2 \lambda/D \times 2 \lambda/D$ square-shaped field centered anywhere from 3 to $\sim 15 \lambda/D$ from the star, and at an arbitrary azimuth, representative of the position of a putative exoplanet.

7.3.3.a. The image is normalized to the “star brightness” as defined in 7.2, using the fixed ratio between peak star brightness and the integrated light in a region of the speckle field outside the central DM-controlled area. I.e., $\text{dark-hole/star} = \text{dark-hole/speckle} * \text{speckle/star}$. For this purpose, any well-defined region of the outer speckle field can be used.

7.3.3.b. The intensity measurement at the output of the SMF is normalized to the “star brightness” as defined in 7.2.3.b.

7.4 Milestone demonstration procedure

7.4.1. The DM is set to scratch. An initial coronagraph contrast field image or SMF measurement is obtained as described in Sec. 7.3.

7.4.2. Wavefront sensing and control is performed to find settings of the DM actuators that give the required high-contrast in the target dark field or through the SMF. This iterative procedure may take from one to several hours, starting from scratch, if no prior information is available. However it can take more or less time depending on the stability of the optical system.

7.4.3. A number of contrast field images or SMF measurements are taken, following steps 7.4.1 – 7.4.2. A sufficient number (≥ 4) of images are taken to provide statistical confidence that the milestone contrast levels have been achieved, as described in Section 7.1.

7.4.4. Laboratory data are archived for future reference, including all raw images and SMF output measurements of the reference star and contrast field.

7.5 Milestone data package

7.5.1. A narrative report that includes a discussion of how each element of the milestone was met, with a narrative summary of the overall milestone achievement and its repeatability.

7.5.2. A description of the optical elements, including the coronagraphic masks, fibers and their significant characteristics.

7.5.3. A tabulation of the significant operating parameters of the apparatus.

7.5.4.a A representative contrast field image or SMF output measurements from the set of images/measurements used in the statistical analysis of the milestone, with appropriate numerical

contrast values indicated, with coordinate scales indicated in units of Airy distance (λ/D) where applicable.

7.5.4.b The mean contrast field image or measurement for the set of images/measurements used in the statistical analysis of the milestone, with appropriate numerical contrast values indicated, with coordinate scales indicated in units of Airy distance (λ/D) where applicable

7.5.5. A description of the data reduction algorithms, in sufficient detail to guide an independent analysis of the delivered data.

7.5.6. Average and mean contrast values and standard deviations for the data used to satisfy the milestone requirements, including a pixel-by-pixel histogram of contrast values across the dark field when applicable.

8 Success Criteria

The following are the required elements of the milestone demonstration. Each element includes a brief rationale.

8.1. Illumination is single polarization at a wavelength in the range of $300 \text{ nm} < \lambda < 1000 \text{ nm}$, for 10%, 20%, or 30% bandwidth, depending on the specific milestone.

Rationale: *This milestone is an initial demonstration of the feasibility of the approach at a wavelength in the science band of Exo-C/Habex/LUVOIR.*

8.2. The contrast specified in each milestone in Table 1 shall be achieved within the control radius of the wavefront control system from 3 to $15 \lambda/D$ (OWA).

Rationale: *This provides evidence that high contrast can be achieved for characterizing planets, yet within proven testbed performance capabilities.*

8.3. Criterion 8.2 shall be met with a confidence of 90% or better. Sufficient data must be taken to justify this statistical confidence, and to mitigate system drifts. Measured open-loop raw contrast drifts during quiet times on the HCST are of the order of $1\text{e-}9/\text{hour}$ (primarily due to pointing drift of $0.03 \lambda/D$ rms). Measured drifts on the DST are of the order of $1\text{e-}10/\text{hour}$ (primarily due to Xinetics DM drifts). Repeating measurements during quiet times when the testbeds have settled and subject to minimal disturbances (e.g. foot and car traffic) is by experience the best strategy to minimize drifts. It should be noted that both HCST and DST are in the process of implementing auxiliary WFS systems that should provide an additional layer of stability control. It is unclear at this time whether these systems will be operational for this program, so our primary strategy is to perform sufficient repeated tests during good stability conditions.

Rationale: *Assuming the contrasts have a Gaussian distribution about the mean, this demonstrates a statistical confidence of 90% that the contrast goal has been met.*

8.4. Elements 8.1 – 8.3 must be satisfied on 3 separate occasions with a reset of the wavefront control system software (DM set to scratch) between each demonstration.

Rationale: *This provides evidence of the repeatability of the contrast demonstration.*

The wavefront control system software reset between experimental runs ensures that the different data sets can be considered as independent and do not represent an unusually good configuration that cannot be readily reproduced. For each demonstration, the DM will begin from a "scratch" setting. There is no time requirement for the demonstrations, other than the time required to meet the statistics stipulated in the success criteria. There is no required interval between demonstrations; subsequent demonstrations can begin as soon as prior demonstrations have ended. There is also no requirement to turn off power, open the vacuum tank, or delete data relevant for the calibration of the DM influence function.

9 Schedule

As described in our selected SAT2018 proposal and the table below, our approved TDEM test plan has a duration of three years. We plan to use both the HCST at Caltech and the DST at JPL.

Simulation work will start immediately to inform the prospects of this technology development and the first year of HCST design development activities.

The HCST tests are front-loaded and the DST tests are back-loaded in accordance to the availability of the DST at JPL.

			2020				2021				2022							
Milestones	Facility	Resp.	Q1	Q2	Q3	Q4	Q1	Q2	Q3	Q4	Q1	Q2	Q3	Q4				
FIU design	HCST	Jovanovic, Llop																
FIU DDR	HCST	Jovanovic, Llop, team																
FIU AIV	HCST	Jovanovic, Llop																
Milestone 0	Simulations	Coker, Llop, Ruane, Riggs																
Milestone 1	HCST	Llop, Echeverri, Jovanovic																
Milestone 2	HCST	Llop, Echeverri, Jovanovic																
Milestone 3	HCST	Llop, Echeverri, Jovanovic																
Milestone 4	DST	Llop, Echeverri, Ruane																
Milestone 5	DST	Llop, Echeverri, Ruane																
Milestone 6	DST	Llop, Echeverri, Ruane																
Final report		Mawet, Stark, team																

Table 3. Schedule.

The Caltech HCST testbed is under the control of the PI, Dimitri Mawet, and is available to be used as indicated in the table above.

The JPL DST testbed is available during the third year of our program. We will perform a series of 3-month runs with a month in between for reconfiguration and data analysis.

Finally, we note that the JPL facility team will be responsible for all DST assembly and alignment steps, for all control and dark-hole generation software, and for any upgrades to the DST facility. As a result, the facility team will likely need additional DST time outside of our official TDEM test runs for such work. We will, however, be happy to work with the DST team to mesh our respective tasks in order to optimize the facility schedule.

10 References

Gaudi BS, Seager S, Mennesson B, Kiessling A, Warfield K, Kuan G, Cahoy K, Clarke JT, Domagal-Goldman S, Feinberg L, Guyon O, Kasdin J, Mawet D, Robinson T, Rogers L, Scowen P, Somerville R, Stapelfeldt K, Stark C, Stern D, Turnbull M, Martin S, Alvarez-Salazar O, Amini R, Arnold W, Balasubramanian B, Baysinger M, Blais L, Brooks T, Calvet R, Cormarkovic V, Cox C, Danner R, Davis J, Dorsett L, Effinger M, Eng R, Garcia J, Gaskin J, Harris J, Howe S, Knight B, Krist J, Levine D, Li M, Lisman D, Mandic M, Marchen L, Marrese-Reading C, McGowen J, Miyaguchi A, Morgan R, Nemati B, Nikzad S, Nissen J, Novicki M, Perrine T, Redding D, Richards M, Rud M, Scharf D, Serabyn G, Shaklan S, Smith S, Stahl M, Stahl P, Tang H, Van Buren D, Villalvazo J, Warwick S, Webb D, Wofford R, Woo J, Wood M, Ziemer J, Douglas E, Faramaz V, Hildebrandt S, Meshkat T, Plavchan P, Ruane G and Turner N (2018) arXiv e-prints.

The LUVOIR Team (2018) arXiv e-prints.

Mawet D, Ruane G, Xuan W, Echeverri D, Klimovich N, Randolph M, Fucik J, Wallace JK, Wang J, Vasisht G, Dekany R, Mennesson B, Choquet E, Delorme JR and Serabyn E (2017) *ApJ*, 838:92. doi:10.3847/1538-4357/aa647f.

Llop Sayson J, Ruane G, Mawet D, Jovanovic N, Calvin B, Levraud N, Roberson M, Delorme JR, Echeverri D, Klimovich N and Xin Y (2019) *Journal of Astronomical Telescopes, Instruments, and Systems*, 5(1):1 – 11 – 11. doi:10.1117/1.JATIS.5.1.019004.

Coker, Carl T.; Shaklan, Stuart B.; Riggs, A J E.; Ruane, Garreth (2019), *Journal of Astronomical Telescopes, Instruments, and Systems*, 5(4), 045003. doi:10.1117/1.JATIS.5.4.045003.

Coker C T, Llop Sayson J, Shaklan S, Riggs A J E, Mawet D, Ruane G, Jovanovic N, Echeverri D (2019) in *Techniques and Instrumentation for Detections of Exoplanets IX*, 111171A. doi:10.1117/12.2528569.

Trauger J, Moody D, Gordon B, Krist J and Mawet D (2011) In *Techniques and Instrumentation for Detection of Exoplanets V*, vol. 8151 of , p. 81510G. doi:10.1117/12.895032.

Rauscher BJ, Bolcar MR, Clampin M, Domagal-Goldman SD, McElwain MW, Moseley SH, Stahle C, Stark CC and Thronson HA (2015) In *Optics for EUV, X-Ray, and Gamma-Ray Astronomy VII*, vol. 9602 of , p. 96020D. doi:10.1117/12.2186554.

Mawet D, Murakami N, Delacroix C, Serabyn E, Absil O, Baba N, Baudrand J, Boccaletti A, Burruss R, Chipman R, Forsberg P, Habraken S, Hamaguchi S, Hanot C, Ise A, Karlsson M, Kern B, Krist J, Kuhnert A, Levine M, Liewer K, McClain S, McEldowney S, Mennesson B, Moody D, Murakami H, Niessner A, Nishikawa J, O'Brien N, Oka K, Park P, Piron P, Pueyo L, Riaud P, Sakamoto M, Tamura M, Trauger J, Shemo D, Surdej J, Tabirian N, Traub W, Wallace

J and Yokochi K (2011) In Techniques and Instrumentation for Detection of Exoplanets V, vol. 8151 of , p. 815108. doi:10.1117/12.896059.

Soummer R, Sivaramakrishnan A, Pueyo L, Macintosh B and Oppenheimer BR (2011) , 729:144. doi:10.1088/0004-637X/729/2/144.

Balasubramanian K, White V, Yee K, Echternach P, Muller R, Dickie M, Cady E, Mejia Prada C, Ryan D, Poberezhskiy I, Zhou H, Kern B, Riggs AJ, Zimmerman NT, Sirbu D, Shaklan S and Kasdin J (2015) In Techniques and Instrumentation for Detection of Exoplanets VII, vol. 9605 of SPIE , p. 96050L. doi:10.1117/12.2188954.

Serabyn E, Prada CM, Chen P and Mawet D (2019) Journal of the Optical Society of America B Optical Physics, 36:D13. doi:10.1364/JOSAB.36.000D13.

Krist JE, Shaklan SB and Levine MB (2008) In Space Telescopes and Instrumentation 2008: Optical, Infrared, and Millimeter, vol. 7010 of , p. 701044. doi:10.1117/12.789788.

Krist J, Effinger R, Kern B, Mandic M, McGuire J, Moody D, Morrissey P, Poberezhskiy I, Riggs AJ, Saini N, Sidick E, Tang H and Trauger J (2018) In Space Telescopes and Instrumentation 2018: Optical, Infrared, and Millimeter Wave, vol. 10698 of Society of Photo-Optical Instrumentation Engineers (SPIE) Conference Series, p. 106982K. doi:10.1117/12.2310043.

Stark CC, Cady EJ, Clampin M, Domagal-Goldman S, Lisman D, Mandell AM, McElwain MW, Roberge A, Robinson TD, Savransky D, Shaklan SB and Stapelfeldt KR (2016) In Space Telescopes and Instrumentation 2016: Optical, Infrared, and Millimeter Wave, vol. 9904 of SPIE, p. 99041U. doi:10.1117/12.2233201.

Give'on A, Kern B, Shaklan S, Moody D C, Pueyo L (2007) in Astronomical Adaptive Optics Systems and Applications III, vol. 6691 of SPIE, p. 66910A. doi:10.1117/12.733122

Pueyo L, Kay J, Kasdin N J, Groff T, McElwain M, Give'on A, Belikov R (2009) Applied Optics, 48(32):6296-6312. doi:10.1364/AO.48.006296

Miller K, Guyon O, Males J (2017) Journal of Astronomical Telescopes, Instruments, and Systems, 3(4), 049002. doi:10.1117/1.JATIS.3.4.049002

Borde P J, Traub W A (2006) The Astrophysical Journal, 638, 488B. doi:10.1086/498669.

Beaulieu M, Abe L, Martinez P, Baudoz P, Gouvret C, Valiki F (2017) Monthly Notices of the Royal Astronomical Society, 469(1):218-230. doi:10.1093/mnras/stx636.

Potier A, Baudoz P, Galicher R, Singh G, Boccaletti A (2020) Astronomy & Astrophysics, 635, A192. doi:10.1051/0004-6361/201937015

Jovanovic N, Martinache F, Guyon O, Clergeon C, Singh G, Kudo T, Garrel V, Newman K, Doughty D, Lozi J, Males J, Minowa Y, Hayano Y, Takato N, Morino J, Kuhn J, Serabyn E, Norris B, Tuthill P, Schworer G, Stewart P, Close L, Huby E, Perrin G, Lacour S, Gauchet L, Vievard S, Murakami N, Oshiyama F, Baba N, Matsuo T, Nishikawa J, Tamura M, Lai O, Marchis F, Duchêne G, Kotani T and Woillez J (2015) *PASP*, 127(955):890–910.

Colavita MM, Wallace JK, Hines BE, Gursel Y, Malbet F, Palmer DL, Pan XP, Shao M, Yu JW, Boden AF, Dumont PJ, Gubler J, Koresko CD, Kulkarni SR, Lane BF, Mobley DW and van Belle GT (1999) *ApJ*, 510:505–521. doi:10.1086/306579.

Seo B-J, Patterson K, Balasubramanian K, Crill B, Chui T, Echeverri D, Kern B, Marx D, Moody D, Mejia Prada C, Ruane G, Shi F, Shaw J, Siegler N, Tang H, Trauger J, Wilson D, Zimmer R, "Testbed demonstration of high-contrast coronagraph imaging in search for Earth-like exoplanets," *Proc. SPIE 11117, Techniques and Instrumentation for Detection of Exoplanets IX*, 111171V (2019); <https://doi.org/10.1117/12.2530033>